High-Performance Thermally Conductive Phase Change Composites by Large-Size Oriented Graphite Sheets for Scalable Thermal Energy Harvesting

Si Wu, Tingxian Li, Zhen Tong, Jingwei Chao, Tianyao Zhai, Jiaxing Xu, Taisen Yan, Minqiang Wu, Zhenyuan Xu, Hua Bao, Tao Deng*, and Ruzhu Wang**

Dr. S. Wu, Prof. T. X. Li, Dr. J. W. Chao, T. Y. Zhai, Dr. J. X. Xu, Dr. T. Y. Yan, Dr. M. Q. Wu, Prof. Z. Y. Xu, Prof. R. Z. Wang

Research Center of Solar Power & Refrigeration

School of Mechanical Engineering

Shanghai Jiao Tong University

Shanghai 200240, P. R. China

E-mail: Litx@sjtu.edu.cn; Rzwang@sjtu.edu.cn

Dr. Z. Tong, Prof. H. Bao

University of Michigan-Shanghai Jiao Tong University Joint Institute

Shanghai Jiao Tong University

Shanghai 200240, P. R. China

Prof. T. Deng

State Key Laboratory of Metal Matrix Composites

School of Materials Science and Engineering

Shanghai Jiao Tong University

Shanghai 200240, P. R. China

E-mail: Dengtao@sjtu.edu.cn

This is the author manuscript accepted for publication and has undergone full peer review but has not been through the copyediting, typesetting, pagination and proofreading process, which may lead to differences between this version and the Version of Record. Please cite this article as doi: 10.1002/adma.201905099.

Keywords: phase change composites, expanded graphite, graphite sheet, thermal conductivity, thermal energy harvesting

Efficient thermal energy harvesting using phase change materials (PCMs) has great potential for cost-effective thermal management and energy storage applications. However, the low thermal conductivity of PCMs (K_{PCM}) is a long-standing bottleneck for high-power-density energy harvesting. Although PCM-based nanocomposites with an enhanced thermal conductivity can address this issue, achieving a higher K (> 10 W m^{-1} K^{-1}) at filler loadings below 50 wt % remains challenging. Herein, we demonstrate a strategy for synthesizing highly thermally conductive phase change composites (PCCs) by compression-induced construction of large-size aligned graphite sheets inside PCCs. The millimeter-sized graphite sheet consists of lateral van-der-Waals-bonded and oriented graphite nanoplatelets at the micro-nanoscale, which together with a thin PCM layer between the sheets synergistically enhance K_{PCM} in the range of 4.4 ~ 35.0 W m^{-1} K^{-1} at graphite loadings below 40.0 wt %. The resulting PCCs also demonstrate homogeneity, no leakage and a superior phase change behavior, which can be easily engineered into devices for efficient thermal energy harvesting by coordinating the sheet orientation with the thermal transport direction. Our method offers a promising route to high-power-density and low-cost applications of PCMs in large-scale thermal energy storage, thermal management of electronics, etc.

Thermal energy harvesting using phase change materials (PCMs) can improve energy utilization efficiency and provide cost-effective energy storage and thermal management by absorbing heat from the surrounding environment and solar irradiation, as well as waste heat produced by industrial processes and electronic devices.[1-3] Organic solid-liquid PCMs have been extensively studied due to their appropriate physical and chemical properties and abundance in natural resources.[4-6] However, the low thermal conductivity (TC, generally K_{PCM} <0.5 W m^{-1} K^{-1}) and leakage issue are two long-standing bottlenecks for their broad-scale practical applications.[7-9] Efficient energy storage and thermal management using PCMs require a substantial improvement in K_{PCM} to achieve superior charging-discharging abilities as well as appropriate encapsulation structures.

Introducing nanoscale or micron-sized carbon materials as fillers is the most frequently used way to improve K_{PCM}.[10] Carbon nanomaterials, such as graphite nanoplatelets (GNPs), multilayer graphene (MLG) and graphene, are obtained by mechanically cleaving or chemically exfoliating the layered van der Waals (vdW) material of graphite flakes and generally have a high aspect ratio and ultrahigh intrinsic in-plane TC (K >1500 W m^{-1} K^{-1} at room temperature).[11-15] The thermal conductivity enhancement (TCE, TCE= (K_{comp} - K_{PCM})/ K_{PCM}) is mainly dependent on the filler loading, interface thermal resistance between filler and PCM, and the geometric and dimensional properties of the filler including lateral size, thickness, and sheet orientation.[16-18] Generally, 2D nanofillers have a lateral size on the micrometer scale and a thickness on the nanoscale.[17] When dispersing these individual nanofillers into a PCM, the TCE is always very poor due to the random geometric contact and interface thermal resistance bottleneck, which can be pronounced even when the fillers form a disordered percolation network.[19,20] Additionally, dispersed fillers can cause an unstable TC during solid-liquid phase transitions.[21] To make full use of the geometric and dimensional properties of sheet-like fillers, they are generally assembled and oriented into an aligned structure by pressure-induced compression,[18,22] vacuum-assisted self-assembly/alignment,[23,24] solution casting,[25] mechanical strain,[26] electric-field-assisted orientation,[27] or ice-templated assembly[28-30] to obtain a structurally anisotropic framework. The individual fillers act as building blocks of the framework, which serves as the thermally conductive matrix in a composite. Thermally conductive polymer-based composites using an aligned GNP framework have been developed for thermal interface materials (TIM).[18,23-27,29] The reported K_{comp} at near room temperature can reach approximately 17 W m^{-1} K^{-1}.[24] Although the TC of composites with an anisotropic framework has been significantly enhanced, the thermal resistance (R) between adjacent building blocks is still high

owing to the incompact contact or possible existence of polymer or PCM, which generates a high-thermal-resistance junction. Such a thermal-resistance junction exhibits a high lateral spatial density because of the micro-nano scale of its building blocks. Both of the thermal-resistance junctions and their high lateral spatial density contribute to the high total in-plane thermal resistance inside bulk composites. Therefore, the size of the aligned sheet-like building blocks plays a significant role in the TCE by affecting the lateral spatial density of the thermal-resistance junctions. Generally, the reported large-area graphite sheets such as GNPs, MLG or graphene have a lateral size smaller than 50 μm.[18,25] Using a graphite sheet with a larger lateral size to decrease the lateral spatial density of high-thermal-resistance junctions can essentially improve the in-plane TCE. However, current engineering technologies, based on mechanically cleaving or chemically exfoliating natural graphite flakes into GNPs, MLG, or graphene, intrinsically destroy the vdW bonding and thus are difficult to synthesize scalable high-quality large-size/area graphite sheet.[31] The CVD-grown growth method can produce such a graphite sheet, but it is generally at a high cost.[32,33]

Herein, we report a strategy to boost the TCE by constructing large-size aligned graphite sheets inside PCCs. The formation of aligned graphite sheets is attributed to mechanically compressing a graphite production—worm-like expanded graphite (WEG) from a natural graphite flake. The graphite sheet with a lateral size at the millimeter scale is composed of highly oriented and vdW-bonded GNPs at the micrometer scale. The vdW interactions between adjacent GNPs can weaken the phonon scattering at the interface due to the adhesion energy (typically less than 100 mJ m^{-2}), which contributes to reducing the interfacial thermal resistance (also known as Kapitza thermal resistance) and to enhancing the nanoscale thermal conduction.[34] In this case, each graphite sheet serves as an independent conductive chain. Before the compression operation, the GNPs on WEG

are coated with a PCM layer. Notably, the PCM layer between adjacent graphite sheets is thin, which causes a low junction thermal resistance. Such a low junction thermal resistance and its low spatial density owing to the large-size graphite sheet synergistically contribute to the high thermal conductivity of the PCCs in a range of 4.4 ~ 35.0 W m^{-1} K^{-1} at graphite loadings below 40.0 wt %. In addition, the resultant PCCs demonstrate a leakage-poof, form-stable and superior phase change behavior, which can be easily engineered into low-cost and scalable thermal energy harvesting devices.

Different from conventional studies which are devoted to processing the natural graphite flake into individual GNPs or graphene nanosheets at the micro-nano size by destroying the inherent vdW interactions,[15,35] **Figure 1** shows the conceptual design of our PCCs. Imaginably, a single natural graphite flake composed of many compact and ordered GNPs can be unfolded by some way into a large graphite sheet composed of GNPs (or single-layer graphene) with lateral vdW bonding (Figure 1a-b). The PCM, which is able to wet a graphite surface when melting, as superfine particles adhere to the surface of graphite sheets. The PCM coating forms after the particles go through a melting-solidification process (Figure 1c-d). Subsequently, it is possible to generate layered composites by the compression-induced assembly of a mass of graphite sheets with the PCM coating (Figure 1e-f). The constitutive GNPs of the graphite sheet become highly oriented after the compression operation, and aligned graphite sheets emerge at the same time (Figure 1g). The sheet-sheet thermal resistance junction in bulk composites would have a low lateral spatial density due to the large-size graphite sheets. In addition, such junction thermal resistances could be at low values owing to the thin PCM layers between adjacent sheets, which are caused by the initial thin PCM coating and the compression operation.

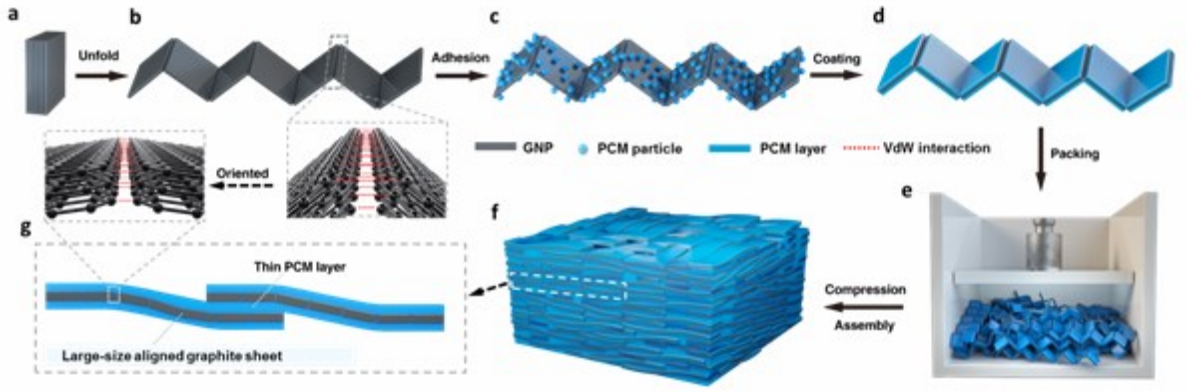

Figure 1. Schematic diagram for synthesizing PCCs and constructing large-size aligned graphite sheets.

The graphite sheet can have a very large area or length according to the exfoliation degree or GNP thickness. When the thickness of a GNP is reduced to single-carbon-atom thickness, the graphite sheet would become a gigantic graphene nanosheet. For the extreme case where the graphite sheet and PCM form separate and well-organized layered composites. No lateral sheet-sheet junction thermal resistance exists inside the composites, and thus the composites possess the theoretically maximum in-plane TCE. A detailed discussion is given in Supplementary Text. In this case, the in-plane K_{comp} can reach up to 10 W m^{-1} K^{-1} even when the volume fraction of the sheet is as low as 1%, and TCE reaches nearly 5000% (typically, K_{PCM} is approximately 0.2 W m^{-1} K^{-1}).

Currently, it is technically difficult to produce the abovementioned graphite sheet from natural graphite flakes (Figure 1b). Alternatively, a piece of GNP cluster can be generated from a piece of graphite flake treated with intercalation compounds by thermal exfoliation. The thermal exfoliation process is to partly preserve the vdW interfaces between GNPs, and the resultant GNP cluster is generally called worm-like expanded graphite (WEG).[35] During this process, the compact and ordered micron-sized GNPs are separated into a piece of WEG (**Figure 2**a and b, and Figure S1). The

interspace between GNPs is extended, and consequently the size (or thickness) of the graphite flakes along the *c*-axis direction increases by more than 100 times, while the diameter remains nearly unchanged after the thermal exfoliation. The loose GNPs on WEG disorderly connect to each other via vdW interactions. Due to the heat treatment during exfoliation, WEG possesses a very low oxygen content and the carbon content is more than 98% (Figure S2). Next, we employ two frequently used hydrophobic organics, stearic acid (SA) and paraffin wax (PW), as PCMs to synthesize two kinds of PCCs. The PCM particles with the diameter in the range of 5 - 30 μm are gently mixed with WEG in proportion where the PCM particles are uniformly dispersed into the cracks or grooves of WEG (Figure S3). The heat treatment melts the PCM to achieve the heat-assisted impregnation of liquid PCM into the extended interspaces of WEG. Because the constitutive GNPs are hydrophobic, the molten PCM can readily adhere to the graphite surfaces (Figure S4). Consequently, the PCM would uniformly coat on the GNPs or/and fill the interspaces between the GNPs. The inherent microstructure of WEG remains almost unchanged after the PCM coating is formed (Figure 2c). Then, a large number of WEG impregnated with PCM are moved into a mold and compressed into a composite block with the desired packing density (Figure 2d-e) at an appropriate temperature, slightly lower than the solidification temperature of the PCM. The GNPs in the composite block are highly oriented and form continuous graphite sheets during the compression process (Figure 2f). Every WEG forms several interconnected graphite sheets consisting of many oriented and vdW-bonded GNPs, which serve as thermally conductive chains inside the composite block. At the bulk level, an aligned and interconnected GNP framework is formed in which some sloping GNPs interconnect the aligned graphite sheets after removing the PCM from the composites by a high-temperature treatment (Figure 2g). The thickness of the constitutive GNPs varies from

approximately 50 nm to 400 nm. Moreover, the oxygen mappings of WEG with the PCM coating and the composite block confirm that the PCM uniformly coats the GNPs (Figure S5).

The XRD pattern for the PCC exhibits three main diffraction peaks, which represent the combination of the one from WEG and the two from the PCM with a reduction in the intensity for all three peaks (Figure 2h). Similarly, the FT-IR spectrum of the PCC also supports the combination of the PCM and WEG (Figure 2i). These results confirm that the PCC is just the physical integration of the PCM with GNPs, and no chemical reaction occurs. The nitrogen isothermal sorption results reveal that the specific surface area of WEG is approximately 61.9 $m^2 g^{-1}$, and the micropores of WEG disappear after coating the GNPs with the PCM (Figure 2j). Moreover, the specific surface area and average pore volume of WEG with PCM coating successively decrease with the increment of PCM content (Table S1), which indicates that the PCM coating layer becomes thicker and/or the filling degree of interspace between GNPs is higher at a lower WEG loading. According to the data of the specific surface area, we can roughly estimate the thickness of the PCM coating layer in the range of 110 ~370 nm when the WEG loading varies from 40 wt% to 20 wt%.

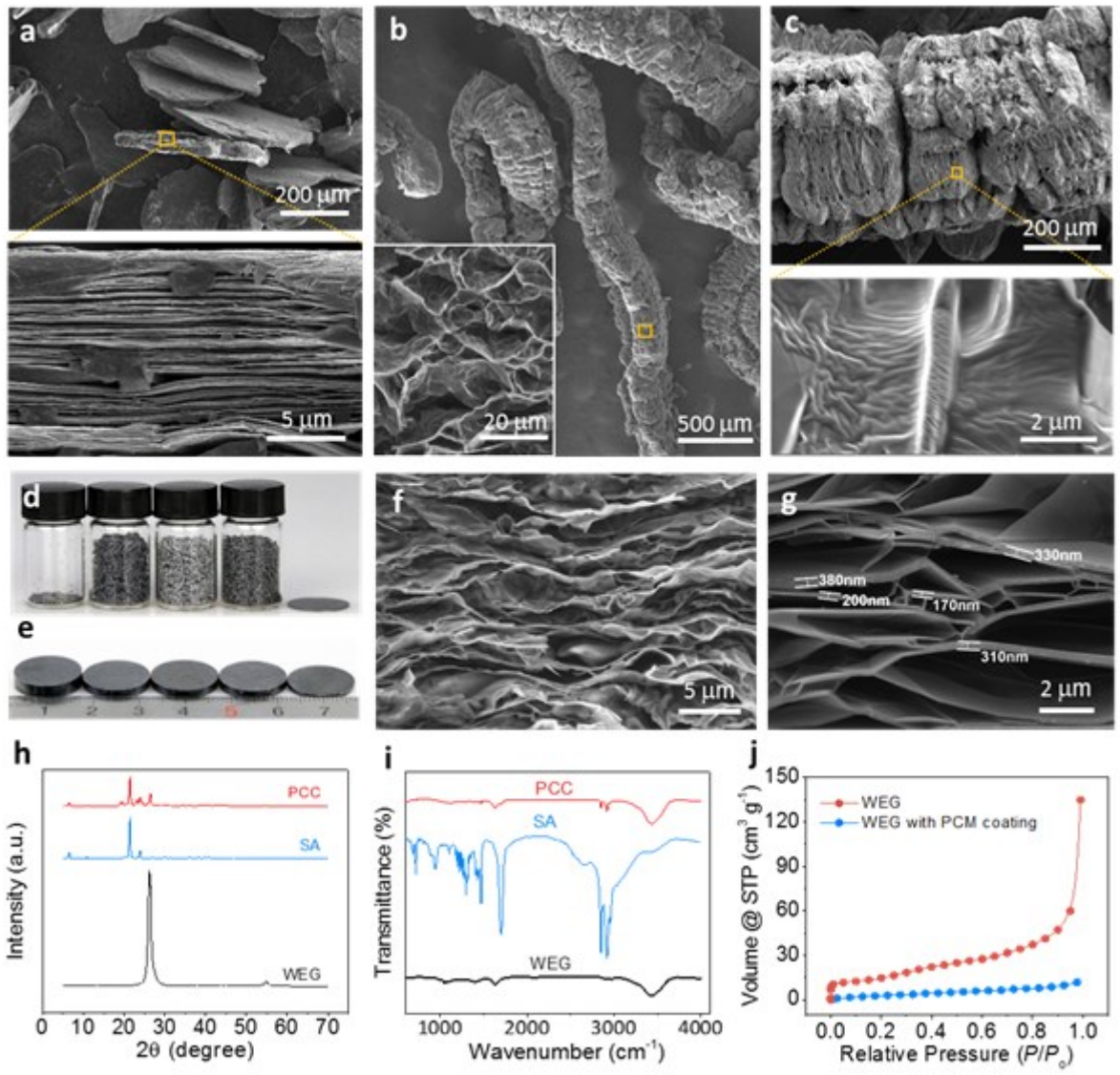

Figure 2. Morphology and structural characterizations of the PCC based on SA. (a) The SEM image of the graphite intercalation compounds. (b) The SEM image of WEG. (c) The microstructure of WEG with the SA coating. The magnification shows the PCM coating layer. (d) The digital photo of the graphite intercalation compound, WEG, WEG adhered with SA particles, WEG with the SA coating and the compressed composite disc (from left to right). (e) The digital photo of composite blocks with different thicknesses. (f) The SEM image of a broken composite block from the side view. (g) The SEM image of a 3D aligned and interconnected GNP framework after removing the PCM from composite block. (h) XRD and (i) FT-IR spectrum results for WEG, SA and the WEG/SA composite. (j)

N_2 isothermal sorption curves of raw WEG and WEG with the SA coating at a graphite loading of 20.0 wt%.

Most studies on composites with thermally conductive filler have been limited to a relatively low filler loading fraction, $\phi \leq 10$ vol%, due to the difficulties in the preparation of high-loading composites with a uniform dispersion.[11,18] The changes in viscosity and filler agglomeration complicate the synthesis of composites with a loading above 10 vol %.[20] Herein, our method can easily synthesize composites with a high filler loading, beyond the PCM-based composite, due to the absence of a significant viscosity and filler agglomeration. Furthermore, the minimum filler loading depends on the maximum adhesive capacity of the PCM on WEG, which is approximately 4 wt% in this work. Our method also offers an effective and low-cost route to fabricate large-scale and homogenous PCC blocks due to the absence of a considerable capillary resistance when compared to other conventional methods in which highly thermally conductive carbon matrices are firstly prefabricated and then infiltrated with the liquid PCM/polymer.[8-10,24,28,29,36-40] Furthermore, our method can easily tailor the thermal properties of PCCs by independently adjusting the graphite loading and packing density. For a certain graphite loading, the packing density should not exceed the leakage alarm density in consideration of the volume change of the PCM during the solid-liquid phase transition.

It is widely known that structural anisotropy causes an anisotropic thermal conductivity. In this work, we only focus on the enhancement of the in-plane thermal conductivity of PCCs (along the alignment of the graphite sheets). To investigate the size effect of the graphite sheet on the TCE, we firstly compared the TCs of different compressed graphite blocks made from WEG and WEG

ultrasonically pulverized for 15 min, 30 min, and 60 min (named as 15-WEG, 30-WEG and 60-WEG). The ultrasonic treatment destroys the vdW interactions between adjacent GNPs and is generally used to further exfoliate WEG into individual GNPs or MLG.[11-13,35] The average length and diameter of raw WEG are 2.2 mm and 0.5 mm respectively (Figure S6). A longer ultrasonic treatment time means smaller-scale GNP stacks and shorter graphite sheets after compression (Figure S7). As shown here, the in-plane TCs of compressed WEG blocks ($K_{C\text{-}WEG}$) and 15-WEG blocks ($K_{C\text{-}15\text{-}WEG}$) at room temperature increase with the packing density (**Figure 3**a). Noteworthily, $K_{C\text{-}WEG}$ is always higher than $K_{C\text{-}15\text{-}WEG}$ for a given packing density, and the in-plane TCs of samples subjected to increased ultrasonic treatment from 0 min to 60 min successively decrease from 194.8±7.0 W m^{-1} K^{-1} to 97.6±5.1 W m^{-1} K^{-1} while at nearly the same packing density.

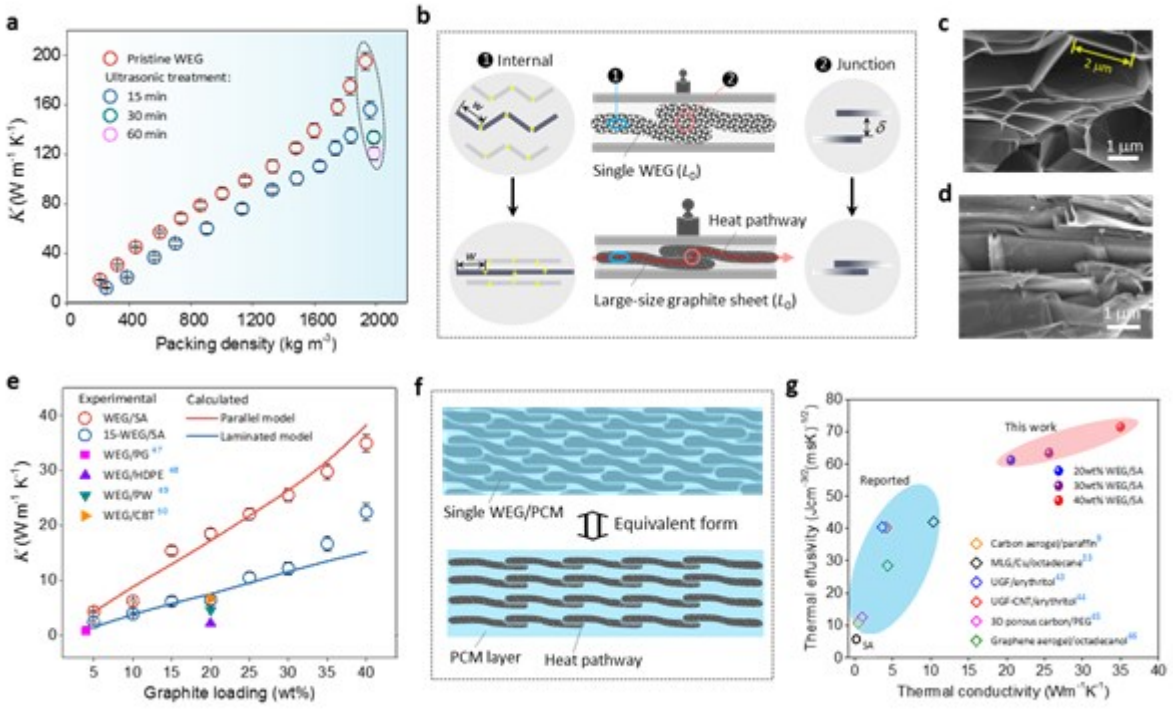

Figure 3. In-plane thermal conduction characteristics of compressed graphite blocks and composite blocks at room temperature. (a) The in-plane TCs of four kinds of compressed graphite blocks as a function of the packing density. (b) The configuration diagram of compressed WEG. The red circles represent the thermal-resistance junctions between adjacent WEGs (or graphite sheets). The blue ellipses represent the partial WEGs (or graphite sheets). The red arrows represent the heat flow. The yellow semitransparent solid circles represent the connections between GNPs. The SEM images of WEG blocks at a low (c) and high (d) packing density from the side view. (e) In-plane TCs of WEG/SA and 15-WEG/SA composite blocks as a function of the graphite loading. The packing densities of all composites are controlled at the leakage alarm density. The parallel model and laminated model are explained in Supporting Information. (f) Schematic diagrams of the parallel model for the thermal conduction inside composites. (g) A comparison of the thermal effusivity and TC of PCCs from the latest reports. Some reports did not mention the density of the PCC. Herein, we calculate the probably maximum thermal effusivity of the PCCs by using the maximum density of the composite block, assuming the PCM and carbon matrix are perfectly mixed and there are no pores existing inside the composite blocks.

Considering two pieces of WEG as the study object and thermal conduction in a one-dimensional case, the constitutive GNPs are oriented and thus the WEGs are aligned into large-size graphite sheets during the compression process (Figure 3b). For an extreme case where all the GNPs are completely oriented, the total lateral thermal resistance consists of the junction thermal resistance (R_{junction}) between sheets and thermal resistance of sheet itself (R_{sheet}):

$$R_{\text{sheet}} \approx \frac{L_0}{w}(R_{\text{g/g}} + R_{\text{g}}) = \frac{L_0}{w} R_{\text{g/g}} + \frac{L_0}{K_{\text{g}}} \quad (1)$$

where $R_{\text{g/g}}$ and R_{g} are the vdW interface thermal resistance and intrinsic thermal resistance of the GNP itself. L_0 and w are the average effective length of the graphite sheet and GNP, respectively. L_0 varies from the diameter of the WEG to its length, depending on the orientation before compression. L_0/w represents the number of vdW interfaces between GNPs. K_{g} is the intrinsic

thermal conductivity of a GNP. Therefore, the thermal conductivity of a single graphite sheet (K_{sheet}) can be expressed as:

$$K_{sheet} = \frac{L_0}{R_{sheet}} \approx \frac{1}{(\frac{1}{w})R_{g/g} + \frac{1}{K_g}} \quad (2)$$

where we define $1/w$ as the in-plane spatial density of the GNP-GNP vdW interface. $R_{g/g}$ is generally very low, at the order of 10^{-9} K m^2 W^{-1}.[12,41] Thus, K_{sheet} can be of magnitude 10^2 - 10^3 W m^{-1} K^{-1} when considering w at 10^{-6} m (approximately 2 μm, as shown in Figure 3c) and K_g at 10^3 W m^{-1} K^{-1}.[14] Similarly, for a very small overlap length of adjacent graphite sheets, the thermal conductivity of the heat pathway constituting several graphite sheets can be expressed as:

$$K_{pathway} \approx \frac{1}{(\frac{1}{L_0})R_{junction} + \frac{1}{K_{sheet}}} \quad (3)$$

where $R_{junction}$ is the thermal resistance between adjacent graphite sheets, $1/L_0$ is the in-plane spatial density of sheet-sheet junction, and $K_{pathway}$ can be considered as the in-plane TC of the graphite block using WEG due to its lack of dependence on the length of the heat pathway. The measurement results confirm $K_{pathway}$ at an order of magnitude of 10^2 W m^{-1} K^{-1} at a packing density above 1500 kg m^{-3}.

As shown in Figure 3c and d and Figure S8, the increased packing density due to the high pressure results in a better orientation of the constitutive GNPs and a closer attachment of adjacent sheets, which indicates a smaller gap (δ) between graphite sheets to decrease the sheet-sheet junction thermal resistance, $R_{junction}$. Consequently, the in-plane TC of the graphite block increases with the

packing density. In addition, a longer graphite sheet from WEG contributes to a lower in-plane spatial density ($1/L_0$) of the sheet-sheet junction than do those obtained from ultrasonically pulverized WEG, which also cause a higher in-plane TC. Evidently, the lateral size of WEG or a graphite sheet (> 2 mm) is approximately three orders of magnitude larger than that of its constitutive GNPs (~2 μm). Similar results have been reported by Balandin et al. who investigated the thermal conductivity of uncompressed and compressed graphene laminates using graphene flakes with different lateral sizes.[42]

In the same way, PCCs using WEG always exhibit a higher in-plane TC than do those using 15-WEG at the same graphite loading (Figure 3e). When the graphite loading is 20.0±0.1 wt%, the in-plane TC of the WEG/SA composites, 17.8±1.8 W m^{-1} K^{-1}, is more than twice that of the 15-WEG/SA composites and approximately 100 times higher than that of pure SA, 0.18 W m^{-1} K^{-1}. In addition, the in-plane TC of the WEG/PW composites with a graphite loading of 20.0±0.1 wt% is 18.1±1.6 W m^{-1} K^{-1}, which is close to that of the WEG/SA composites.

We use different calculation models to match the experimental TC. The parallel model fits the TC of WEG-based composites well, while the laminated model matches that of 15-WEG-based composites well (Figure 3e and Figure S9). Detailed discussions are demonstrated in Supporting Information. From the view of the physical meaning of the two models, the parallel model is an extreme case of the laminated model, and it combines K_{pathway} and K_{PCM} through a weighted mean according to the volume fraction (ϕ):

$$K_{\text{comp, in-plane}} = \phi K_{\text{pathway}} + (1-\phi) K_{\text{PCM}} \quad (4)$$

This indicates that the WEG-based composite block has thermally conductive pathways similar to those in the compressed WEG block and thus achieves the maximum TCE. The physics of thermal conduction inside the composites is formally equivalent to that inside the layered materials with the separated PCM layers (K_{PCM}) and layers of the compressed WEG block ($K_{pathway}$) (Figure 3f).

The laminated model highlights the thermal resistance between the filler and PCM, which predominates the overall thermal resistance of the 15-WEG-based composites. The previously reported composites using WEG as a filler had thermal conductivities close to those of the 15-WEG-based composites (Figure 3e), which indicated that the contribution of WEG to the TCE in other studies was limited.[47-50] That is because the microstructure of WEG in these reports was destroyed due to inappropriate treatments such as ball milling,[47] high-speed grinding,[48] drastic magnetic stirring or ultrasonic treatment.[49] Further comparisons are demonstrated in Table S4.

Apart from the high thermal conductivity, our PCCs also demonstrate a suppressed supercooling degree $\Delta T_{sc} < 2$ °C (defined as the difference between the melting temperature, T_m, and solidification temperature, T_s; $\Delta T_{sc} = T_m - T_s$) and a stable phase change behavior (Figure S10 and Figure S11). The WEG has a negligible effect on the intrinsic specific heat of fusion of the PCM (Table S5 and Table S6). The composite blocks with graphite loadings higher than 5 wt% show no liquid leakage and reveal a stable macro-morphology (Figure S12 and Figure S13), which is attributed to capillary action and the appropriate packing density. Hence, the graphite loading should be higher than 5 wt% when shape-stable and leakage-proof PCCs are desired. Furthermore, no evident weight loss or decomposition reactions occur in the range from 25 °C to 180 °C (Figure S14). The thermal expansion measurement indicates that the in-plane thermal expansion is less than 0.5% (Figure S15).

Figure 3g shows a comparison of the thermal effusivities (defined as the square root of the product of TC, density (ρ) and the phase change enthalpy (ΔH); $e = \sqrt{K\rho\Delta H}$), which represent a material's ability to exchange thermal energy with its surroundings.[33] In comparison with the latest reports, our PCCs exhibit a substantially higher room-temperature TC and thermal effusivity by a factor approximately 2~6.[9,33,43-46]

In view of the alignment structure of graphite sheets inside a PCC, we demonstrate a heat design strategy to achieve high-power-density energy harvesting devices by coordinating the graphite sheets with 1D/2D heat transfers in leakage-proof composites. Firstly, we experimentally compare the thermal charging powers of a WEG/SA composite block under 1D coordinated/uncoordinated heat conduction. When the heat transports along the alignment of the graphite sheets, the thermal charging power is more than twice that across the alignment (**Figure 4**a and b).

For the thermal energy storage application, we design a thermal energy harvesting device to supply/extract heat to/from the WEG/SA composites by a heat transfer fluid (Figure 4c). This device consists of the composite block and a heat exchange tube (copper tube). The compression direction of the composite block is maintained in accordance to the axial direction of the tube to coordinate the alignment of the graphite sheets and the heat conduction. The detailed introduction is provided in Supporting Information. In this case, the compact compression generates horizontal force which is beneficial to weaken the thermal contact resistance ($R_{contact}$) between the copper tube and composite block. A thermal energy harvesting device with a 1 kWh heat capacity is fabricated, and its thermal cycling performance is tested (Figure 4d and Figure S16). The heat capacity remained stable after more than 100 charging/discharging cycles, and its energy density is approximately 51

kWh m^{-3}. Moreover, a large-scale thermal energy storage system with different storage capacities can be easily custom-made by assembling the thermal energy harvesting devices.

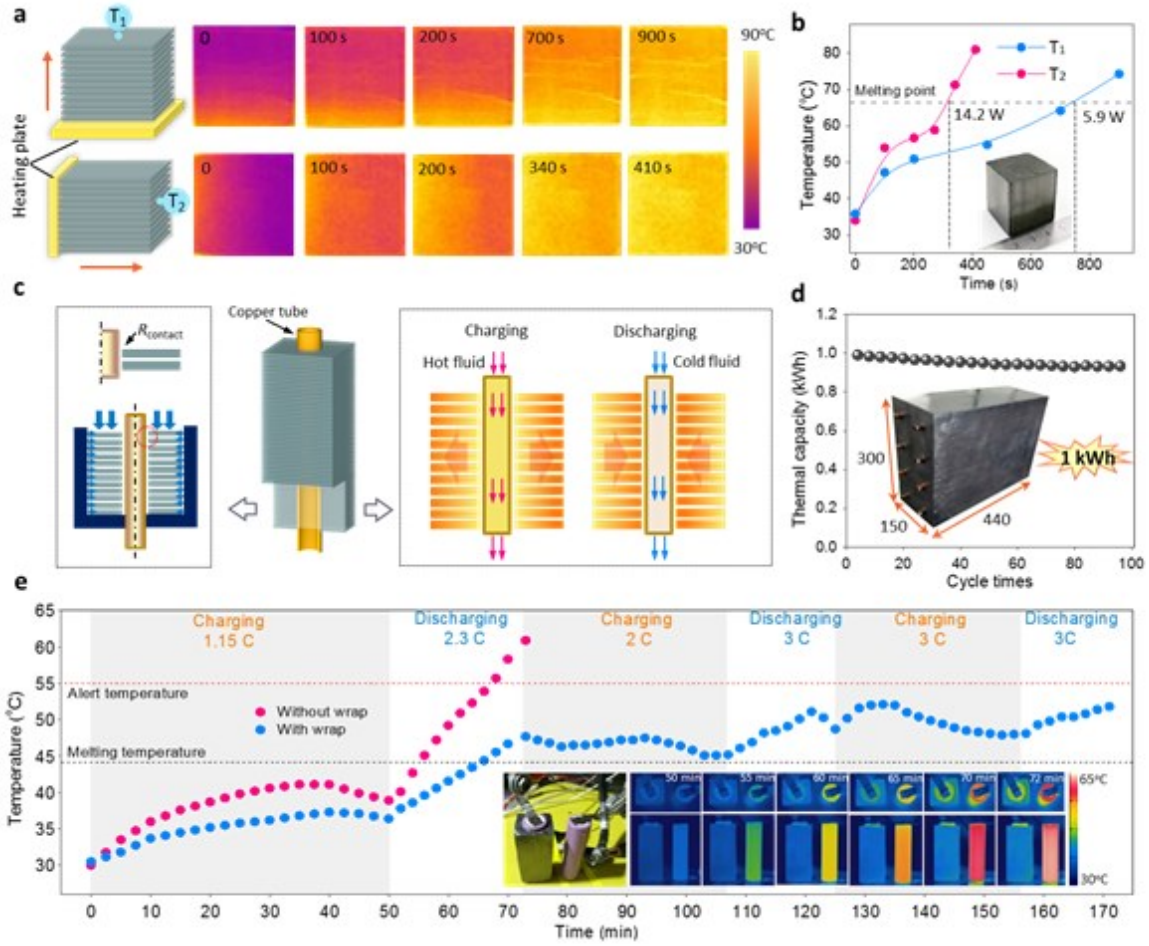

Figure 4. Thermal management and energy storage applications. (a) A comparison of 1D coordinated and uncoordinated heat conduction. The temperature of the heating plate is maintained at 90 °C. (b) The temperature profiles of the measured points. The inset is a digital photo of the composite block. (c) A schematic diagram of the heat design for the thermal energy harvesting device. (d) The thermal capacity stability of the thermal energy harvesting device. The inset is a digital photo of the thermal energy harvesting device with a size of millimeters. (e) Temperature profiles for two battery monomers. The insets show the digital photos of tested battery monomers and their infrared images during the discharging process from 50 min to 72 min.

For the thermal management application, we develop a high-power-density temperature-control device using the leakage-proof WEG/PW composite block to regulate the working temperature of a commercial 18650 lithium-ion battery monomer. The detailed introduction is given in Supporting Information. We compare the temperature profiles of two battery monomers during the charging/discharging processes. The infrared images show that the maximum surface temperature of the wrapped monomer only reaches 47.8 °C at a discharging rate of 2.3 C (Figure 4e). However, the non-wrapped one reaches 61.0 °C. Further measurements show that the temperature of the wrapped monomer can remain below 55 °C and maintain a uniform distribution, even at a higher charging/discharging rate (3C). Therefore, the thermal management device can significantly prolong the working time of the battery and ensure its high working performance.

In summary, we demonstrate a method to achieve a high TCE for PCCs by the compression-induced construction of large-size aligned graphite sheets inside composites. The thermally conductive sheets consist of highly oriented GNPs bonding via vdW interactions and exhibit a lateral size three orders of magnitude greater than that of conventional individual GNPs. This achievement together with the low thermal resistance between adjacent sheets synergistically contribute to the exceptional TCE. The thermal conductivity of PCCs can be tailored in a range of 4.4 ~ 35.0 W m^{-1} K^{-1} at graphite loadings below 40.0 wt %. Our PCCs also show homogeneity, no leakage and a superior thermal performance. Furthermore, we demonstrate high-power-density energy harvesting devices for the thermal management of power battery and scalable thermal energy storage applications. The present work provides insights into the high thermal conduction enhancement of composites using sheet-like fillers, which are not limited to PCM-based composites but can also be applied to polymer-

based thermal interface materials and to the design of scalable and high-power-density energy harvesting devices for thermal management and energy storage.

Experimental Section

Materials: The graphite intercalation compounds (mesh 50, type KP-100) were purchased from Shanghai Yi Fan Graphite Co. Ltd., China. They were firstly washed with deionized water at room temperature and dried at 120 °C at air atmosphere for 20 h to remove the moisture; then, the samples were subjected to a heat treatment in an electric furnace at 750 °C for approximately 15 min.[51] The ultrasonic treatment was performed to tear WEG into smaller GNP stacks. The ultrasonic processing was performed at 450 W for 15 min, 30 min, and 60 min to obtain GNP clusters at different scales. The sheet-like analytical reagent stearic acid (SA) and paraffin wax (PW) were purchased from Sinopharm Chemical Reagent Co. Ltd., China. The materials were firstly ground into micron-sized SA (PW) particles at room temperature.

Preparation of PCCs: Mix the WEG with SA (PW) particles at a certain mass ratio and then gently stir the mixture to make the SA (PW) particles uniformly adhere to the WEG. The mixture was then placed into an electrical furnace for a heat treatment at 100 °C for approximately 30 min—until the SA (PW) was completely molten. The incompact WEG/SA and WEG/PW composites were transferred into a steel mold and compressed into composite blocks at approximately 60 °C (35 °C) using a hydraulic device at pressures as high as 20 MPa. Similarly, the 15-WEG-based composite blocks were synthesized with different graphite loadings and packing densities. The disc-shape samples presented a diameter of 15 mm and a series of thicknesses from 0.2 mm to 3.0 mm, while the rectangle-like samples were at size of 31 mm ×31 mm ×14 mm.

Characterizations: SEM images were obtained using FE-SEM (field-emission scanning electron microscopy, Sirion 200 instrument, FEI Company, USA) equipped with EDS (energy disperse spectroscopy, INCA X-Act). The XRD patterns were measured with a poly-functional X-ray diffractometer (3 kW/*D8 ADVANCE Da Vinci, Germany) using Cu Kα radiation. FT-IR spectra were obtained using a Nicolet 6700 (Thermal scientific Inc. USA) between 400 cm^{-1} and 4000 cm^{-1}. The contact angles of the molten PCMs on graphite surface were tested using Drop Shape Analyzer (DSA100, KRÜSS GmbH, Germany). The N_2 sorption isotherm curves were measured using a gas sorption analyzer (24/Autosorb-IQ3, China). The thermal diffusivities were directly measured using the laser flash method (LFA 447 flash thermal diffusivity instrument; NETZSCH Company, Germany). The thermal conductivity was calculated using the equation $K = \alpha \times C_p \times \rho$, where α is the thermal diffusivity, C_p the specific heat capacity, and ρ the density of the sample. The sample density was measured by a density balance (METLER TOLEDO XS204, Toledo Scale Company, USA) at room temperature. The phase change temperatures, specific heat capacity and heat of fusion were measured by a differential scanning calorimeter (Pyris1 DSC, Perkin-Elmer, Inc., USA) with a heating/cooling rate at 5 °C min^{-1}. The thermal decomposition was tested by a thermogravimetric analyzer (Pyris1 TGA, Perkin-Elmer, Inc., USA). The heating rate was kept constant at 10 °C min^{-1} under a constant stream of nitrogen at a flow rate of 100 ml min^{-1}. The leakage-proof measurements were performed using a high-precision electronic scale and an electric oven. The thermal expansion measurements were performed by a dilatometer (DIL 402 Expedis, NETZSCH Company, Germany). The IR thermal graphic images were obtained by an infrared camera (FLIR T660, FLIR Company, USA).

Supporting Information

Supporting Information is available from the Wiley Online Library or from the authors.

Acknowledgements

S. Wu and T. X. Li contributed equally to this work. This work was supported by the National Natural Science Foundation of China under the contract No.51876117 and the National Key R&D Program of China under the contract No.2018YFE0100300. Part of this work was funded by the Innovative Research Groups of National Natural Science Foundation of China under the contract No.51521004.

Received: ( )
Revised: ( )
Published online: ( )

References

[1] I. Gur, K. Sawyer, R. Prasher, *Science* **2012**, *335*, 1454.

[2] G. G. D. Han, H. Li, J. C. Grossman, *Nat. Commun.* **2017**, *8*.

[3] Z. Wang, Z. Tong, Q. Ye, H. Hu, X. Nie, C. Yan, W. Shang, C. Song, J. Wu, J. Wang, H. Bao, P. Tao, T. Deng, *Nat. Commun.* **2017**, *8*.

[4] P. Tao, W. Shang, C. Song, Q. Shen, F. Zhang, Z. Luo, N. Yi, D. Zhang, T. Deng, *Adv. Mater.* **2015**, *27*, 428.

[5] K. Kant, A. Shukla, A. Sharma, *Sol. Energ. Mat. Sol. C.* **2017**, *172*, 82.

[6] P. Bose, V. A. Amirtham, *Renewable and Sustainable Energy Reviews* **2016**, *65*, 81.

[7] A. Karaipekli, A. Sarinodot, A. Bicer, *Mater. Lett.* **2009**, 63, 1213.

[8] M. Zhou, T. Lin, F. Huang, Y. Zhong, Z. Wang, Y. Tang, H. Bi, D. Wan, J. Lin, *Adv. Funct. Mater.* **2013**, *23*, 2263.

[9] Y. Wei, J. Li, F. Sun, J. Wu, L. Zhao, *Green Chem.* **2018**, *20*, 1858.

[10] L. Chen, R. Zou, W. Xia, Z. Liu, Y. Shang, J. Zhu, Y. Wang, J. Lin, D. Xia, A. Cao, *ACS Nano* **2012**, *6*, 10884.

[11] A. Yu, P. Ramesh, X. Sun, E. Bekyarova, M. E. Itkis, R. C. Haddon, *Adv. Mater.* **2008**, *20*, 4740.

[12] X. Shen, Z. Wang, Y. Wu, X. Liu, Y. He, J. Kim, *Nano Lett.* **2016**, *16*, 3585.

[13] G. Xin, H. Sun, S. M. Scott, T. Yao, F. Lu, D. Shao, T. Hu, G. Wang, G. Ran, J. Lian, *ACS Appl. Mater. Inter.* **2014**, *6*, 15262.

[14] A. A. Balandin, *Nat. Mater.* **2011**, *10*, 569.

[15] K. S. Novoselov, A. Mishchenko, A. Carvalho, A. H. Castro Neto, *Science* **2016**, *353*, c9439.

[16] X. Xu, L. F. Pereira, Y. Wang, J. Wu, K. Zhang, X. Zhao, S. Bae, B. C. Tinh, R. Xie, J. T. Thong, B. H. Hong, K. P. Loh, D. Donadio, B. Li, B. Ozyilmaz, *Nat. Commun.* **2014**, *5*, 3689.

[17] T. Ma, Z. Liu, J. Wen, Y. Gao, X. Ren, H. Chen, C. Jin, X. L. Ma, N. Xu, H. M. Cheng, W. Ren, *Nat. Commun.* **2017**, *8*, 14486.

[18] H. S. Kim, H. S. Bae, J. Yu, S. Y. Kim, *Sci Rep* **2016**, *6*, 26825.

[19] M. Shtein, R. Nadiv, M. Buzaglo, K. Kahil, O. Regev, *Chem. Mater.* **2015**, *27*, 2100.

[20] F. Kargar, Z. Barani, R. Salgado, B. Debnath, J. S. Lewis, E. Aytan, R. K. Lake, A. A. Balandin, *ACS Appl. Mater. Inter.* **2018**, *10*, 37555.

[21] R. Zheng, J. Gao, J. Wang, G. Chen, *Nat. Commun.* **2011**, *2*, 289.

[22] H. Jung, S. Yu, N. Bae, S. M. Cho, R. H. Kim, S. H. Cho, I. Hwang, B. Jeong, J. S. Ryu, J. Hwang, S. M. Hong, C. M. Koo, C. Park, *ACS Appl. Mater. Inter.* **2015**, *7*, 15256.

[23] N. Song, D. Jiao, P. Ding, S. Cui, S. Tang, L. Shi, *J. Mater. Chem. C* **2016**, *4*, 305.

[24] Q. Li, Y. Guo, W. Li, S. Qiu, C. Zhu, X. Wei, M. Chen, C. Liu, S. Liao, Y. Gong, A. K. Mishra, L. Liu, *Chem. Mater.* **2014**, *26*, 4459.

[25] P. Kumar, S. Yu, F. Shahzad, S. M. Hong, Y. Kim, C. M. Koo, *Carbon* **2016**, *101*, 120.

[26] M. Saeidijavash, J. Garg, B. Grady, B. Smith, Z. Li, R. J. Young, F. Tarannum, N. Bel Bekri, *Nanoscale* **2017**, *9*, 12867.

[27] Y. Guo, Y. Chen, E. Wang, M. Cakmak, *ACS Appl. Mater. Inter.* **2016**, *9*, 919.

[28] J. Yang, L. Tang, R. Bao, L. Bai, Z. Liu, W. Yang, B. Xie, M. Yang, *J. Mater. Chem. A* **2016**, *4*, 18841.

[29] G. Lian, C. Tuan, L. Li, S. Jiao, Q. Wang, K. Moon, D. Cui, C. Wong, *Chem. Mater.* **2016**, *28*, 6096.

[30] J. Yang, X. Li, S. Han, R. Yang, P. Min, Z. Yu, *J. Mater. Chem. A* **2018**, *6*, 5880.

[31] J. Zhao, S. Pei, W. Ren, L. Gao, H. Cheng, *ACS Nano* **2010**, *4*, 5245.

[32] Y. Ma, Y. Chen, *National Science Review* **2015**, *2*, 40.

[33] A. L. Cottrill, A. T. Liu, Y. Kunai, V. B. Koman, A. Kaplan, S. G. Mahajan, P. Liu, A. R. Toland, M. S. Strano, *Nat. Commun.* **2018**, *9*.

[34] J. Yang, Y. Yang, S. W. Waltermire, X. Wu, H. Zhang, T. Gutu, Y. Jiang, Y. Chen, A. A. Zinn, R. Prasher, T. T. Xu, D. Li, *Nat. Nanotechnol.* **2012**, *7*, 91.

[35] A. Celzard, J. Mareche, G. Furdin, *Prog. Mater. Sci.* **2005**, *50*, 93.

[36] X. Py, R. Olives, S. Mauran, *Int. J. Heat Mass Transfer* **2001**, 44, 2727.

[37] A. Mills, M. Farid, J. R. Selman, S. Al-Hallaj, *Appl. Therm. Eng.* **2006**, *26*, 1652.

[38] G. Fang, H. Li, Z. Chen, X. Liu, *Energy* **2010**, *35*, 4622.

[39] L. Zhang, R. Li, B. Tang, P. Wang, *Nanoscale* **2016**, *8*, 14600.

[40] Z. Wu, C. Xu, C. Ma, Z. Liu, H. M. Cheng, W. Ren, *Adv. Mater.* **2019**, *31*, 1900199.

[41] K. M. F. Shahil, A. A. Balandin, *Nano Lett.* **2012**, *12*, 861.

[42] H. Malekpour, K. H. Chang, J. C. Chen, C. Y. Lu, D. L. Nika, K. S. Novoselov, A. A. Balandin, *Nano Lett.* **2014**, *14*, 5155.

[43] H. Ji, D. P. Sellan, M. T. Pettes, X. Kong, J. Ji, L. Shi, R. S. Ruoff, *Energ. Environ. Sci.* **2014**, *7*, 1185.

[44] I. Kholmanov, J. Kim, E. Ou, R. S. Ruoff, L. Shi, *ACS Nano* **2015**, *9*, 11699.

[45] X. Chen, H. Gao, M. Yang, W. Dong, X. Huang, A. Li, C. Dong, G. Wang, *Nano Energy* **2018**, *49*, 86.

[46] J. Yang, X. Li, S. Han, R. Yang, P. Min, Z. Yu, *J. Mater. Chem. A* **2018**, *6*, 5880.

[47] N. Zhang, Y. Song, Y. Du, Y. Yuan, G. Xiao, Y. Gui, *Adv. Eng. Mater.* **2018**, *20*, 1800237.

[48] J. Che, K. Wu, Y. Lin, K. Wang, Q. Fu, *Composites Part A: Applied Science and Manufacturing* **2017**, *99*, 32.

[49] X. L. G. Z. Ziyuan Wang, *RSC Adv.* **2017**.

[50] Y. J. Noh, H. S. Kim, B. Ku, M. Khil, S. Y. Kim, Adv. Eng. Mater. 2016, 18, 1127.

[51] M. Bonnissel, L. Luo, D. Tondeur, *Carbon* **2001**, *39*, 2151.

The table of contents entry should be 50−60 words long and should be written in the present tense and impersonal style (i.e., avoid we). The text should be different from the abstract text.

Phase change composites

Si Wu, Tingxian Li, Zhen Tong, Jingwei Chao, Tianyao Zhai, Jiaxing Xu, Taisen Yan, Minqiang Wu, Zhenyuan Xu, Hua Bao, Tao Deng*, and Ruzhu Wang**

High-Performance Thermally Conductive Phase Change Composites by Large-Size Oriented Graphite Sheets for Scalable Thermal Energy Harvesting

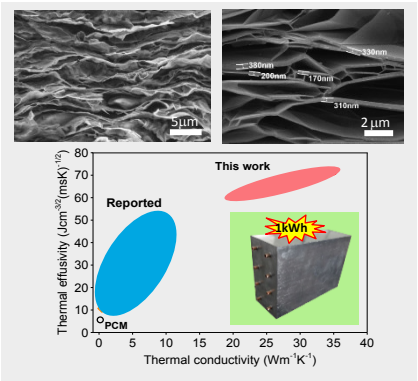

A method for synthesizing high-performance thermally conductive phase change composites is demonstrated. The large-size aligned graphite sheets inside the composite are generated from worm-like expanded graphite. The aligned and interconnected graphite framework enhances K_{PCM} up to 4.4 ~ 35.0 W m^{-1} K^{-1} at graphite loadings below 40.0 wt %, which will accelerate the high-power-density, low-cost and large-scale applications of PCMs.